



Article

Discrete Element Method Analyses of Bond Degradation Evolutions for Cemented Soils

Jie He ^{1,2}, Tao Li ³ and Yi Rui ^{1,2,*}¹ College of Civil Engineering, Tongji University, Shanghai 200092, China; hejie@tongji.edu.cn² State Key Laboratory for Disaster Reduction in Civil Engineering, Tongji University, Shanghai 200092, China³ School of Transportation Science and Engineering, Civil Aviation University of China, Tianjin 300300, China; tli@cauc.edu.cn

* Correspondence: ruiyi@tongji.edu.cn

Abstract: The degradation of soil bonding, which can be described by the evolution of bond degradation variables, is essential in the constitutive modeling of cemented soils. A degradation variable with a value of 0/1.0 indicates that the applied stress is completely sustained by bonded particles/unbonded grains. The discrete element method (DEM) was used for cemented soils to analyze the bond degradation evolution and to evaluate the degradation variables at the contact scale. Numerical cemented soil samples with different bonding strengths were first prepared using an advanced contact model (CM). Constant stress ratio compression, one-dimensional compression, conventional triaxial tests (CTTs), and true triaxial tests (TTTs) were then implemented for the numerical samples. After that, the numerical results were adopted to investigate the evolution of the bond degradation variables B_N and B_0 . In the triaxial tests, B_0 evolves to be near to or larger than B_N due to shearing, which indicates that shearing increases the bearing rate of bond contacts. Finally, an approximate stress-path-independent bond degradation variable B_σ was developed. The evolution of B_σ with the equivalent plastic strain can be effectively described by an exponential function and a hyperbolic function.

Keywords: numerical simulation; discrete element method; cemented soil; bond degradation evolution; bond breakage



Citation: He, J.; Li, T.; Rui, Y. Discrete Element Method Analyses of Bond Degradation Evolutions for Cemented Soils. *Fractal Fract.* **2024**, *8*, 119.

<https://doi.org/10.3390/fractalfract8020119>

Academic Editors: Zine El Abidine Fellah and Carlo Cattani

Received: 10 November 2023

Revised: 9 February 2024

Accepted: 15 February 2024

Published: 17 February 2024



Copyright: © 2024 by the authors. Licensee MDPI, Basel, Switzerland. This article is an open access article distributed under the terms and conditions of the Creative Commons Attribution (CC BY) license (<https://creativecommons.org/licenses/by/4.0/>).

1. Introduction

Soil fabric and interparticle bonding together can be termed soil structure [1]. There are substantial distinctions in the mechanical properties between natural/artificially cemented soils (CSs) and uncemented soils (USs) ascribed to the interparticle bonding derived from cementation, as verified by experimental data [2,3]. Cemented soils exhibit structural yielding in isotropic compression and strain softening in triaxial tests. These characteristics are ascribed to the degradation evolutions of cementation bond contacts. Further, for silt-sized soils, fine particles can sustain themselves in a loose structure due to the van der Waals attraction force [4]. Loose cemented soils may undergo a considerable volume change under loading/wetting due to interparticle bond degradation and may cause engineering problems [5,6]. Accordingly, it is essential to quantify the bonding effect and to assess the bonding degradation evolution when carrying out constitutive modeling of cemented soil.

As a cemented soil is loaded, the interparticle bonds gradually break, and the cemented soil correspondingly performs towards the uncemented soil. A bond degradation variable represents the degree to which the soil bonding is damaged. Although it is complex to model the degree and degradation of interparticle bonding, a variety of formulations have been proposed and incorporated into constitutive models in recent decades. Some models have assumed a larger yield surface for cemented soil, which is progressively reduced during bond degradation. By comparing the yield surface size of cemented soil p_c and the corresponding uncemented soil p_{c0} , the bonding effect can be assessed by evaluating the additional strength $\Delta p_c = p_c - p_{c0}$ [7,8]

or the strength ratio $R^* = p_{c0}/p_c$ [9–11]. Alternatively, in the disturbed state concept [12,13], cemented soil is modeled by a combination of material parts at relatively intact and fully adjusted states. The bonding effect can be quantified by the disturbance function D , which denotes the contribution ratio of fully adjusted states to material stress. In the damage model for cemented soils [14,15], a similar strategy is employed, and the bonding effect can be quantified by a bond degradation variable. However, owing to the difficulties in microscopic observations and the deficiency of the micromechanical basis, these bond degradation indicators that denote the debonding process are based on the macro mechanical differences between cemented and corresponding uncemented soils.

Since it is difficult to obtain insight into the debonding process at the particle and contact scales with current experimental technologies [16–18], the DEM [19] is a supplementary way to study microscopic behavior and analyze the bond degradation evolution of cemented soils. The DEM has been employed in microscopic investigations on various cemented soils, such as cemented sand, structural silt, methane hydrate-bearing soil, etc. [20–25]. The DEM has also been applied to correlate the macro- and micromechanical performances of geomaterials [15,26,27]. Thornton [26] relates the normal and tangential contact forces to the stress tensor, respectively. Jiang et al. [15] relates the forces at bonded contacts and the forces at unbonded contacts to the stress tensor, respectively, and developed micromechanical-based models for cemented soils.

In this study, a numerical sample is first produced using the particle flow code 3D (PFC3D) [28], whose contact model takes into account rolling and twisting resistances [29] and van der Waals forces [30,31] to sustain an open structure, followed by precompression and cementation bond generation. Subsequently, various loading paths, including constant stress ratio compression, one-dimensional compression, conventional triaxial, and true triaxial loading, are applied on cemented DEM assemblies with different bond strengths. After that, the evolution of two representative bond degradation variables versus plastic strain is micromechanically investigated. Finally, the bond degradation evolution of cemented soils not only depends on the plastic strain but also the stress path. Based on the DEM analyses of the bond degradation evolution, an approximate stress-path-independent bond degradation variable and its degradation evolution law are proposed.

2. Materials and Methods

2.1. Bond Contact Model Framework

The force and moment at a contact point between particles are considered to be conveyed through both particle interactions and the bonding material in parallel. The total force (moment) vector is the sum of the force (moment) vector transmitted by the particle interaction and the force (moment) vector transmitted by the cementation bond. The schematic diagram (Figure 1) shows the forces and moments in four directions: normal, tangential, rolling, and twisting.

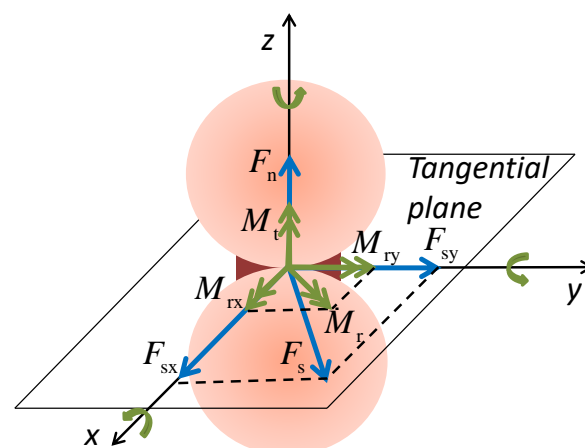


Figure 1. Contact forces and moments in the local coordinate system.

2.1.1. Particle Interaction

A three-dimensional contact model, which accounts for sliding, rolling and twisting resistances [28,29], was employed to account for the influence of particle shapes on sphere-based DEM simulations, and it was then further developed for soils with interparticle attraction forces, such as silt-sized soils with van der Waals forces [30].

The model posits that the interaction between two spheres occurs at the contact through a circular flat region with a specific radius $R_c = \beta R$, where β serves as the shape parameter governing the characteristics of rolling and twisting resistances, $R = 2R_1R_2/(R_1 + R_2)$ represents the shared radius of the particle pair, and R_1 and R_2 are their individual radii, respectively.

In the direction perpendicular to the surface, the normal force is computed by the following:

$$F_n^p = \begin{cases} k_n \delta_n - F_v & \delta_n \geq 0 \\ 0 & \delta_n < 0 \end{cases} \quad (1)$$

where k_n is the normal stiffness, δ_n is the normal overlap between a pair of particles with a negative value denoting separation, and F_v is the van der Waals force.

The tangential force, rolling moment, and twisting torque are determined through incremental calculations as follows:

$$F_s^p \leftarrow F_s^p - k_s \Delta \delta_s \quad (2)$$

$$M_r^p \leftarrow M_r^p - k_r \Delta \theta_r \quad (3)$$

$$M_t^p \leftarrow M_t^p - k_t \Delta \theta_t \quad (4)$$

where k_s , $k_r = 0.25k_n R_c^2$, and $k_t = 0.5k_s R_c^2$ denote the tangential, rolling, and twisting stiffnesses, respectively, and $\Delta \delta_s$, $\Delta \theta_r$, and $\Delta \theta_t$ are the relative shear displacement increment, rotation increment, and twist increment, as introduced in the contact resolution in PFC^{3D} [28]. Tangential sliding is initiated and the contact transitions to the perfectly plastic stage once the tangential force reaches its limiting value, i.e., $\|F_s^p\| \leq \mu(F_n^p + F_v)$, where μ is the friction coefficient between the particles. Similarly, rolling is initiated when the rolling moment attains the limiting value, i.e., $\|M_r^p\| \leq 0.25\zeta_c R_c (F_n^p + F_v)$, where the local crushing parameter ζ_c is 2.1. Plastic twisting is triggered when the torque reaches its limiting value, i.e., $M_t^p \leq 0.65\mu R_c (F_n^p + F_v)$.

The normal and tangential stiffnesses can be calculated in a simple way to consider the effect of particle radii [28]:

$$k_n = \pi R^2 E^* / (R_1 + R_2) \quad (5)$$

$$k_s = k_n / \kappa^* \quad (6)$$

where E^* represents the effective modulus between particles, and κ^* denotes the ratio of normal stiffness to shear stiffness.

2.1.2. Prefailure Behavior of the Cementation Bond

The connection between two spheres can be conceptualized as a short cylinder with concave spherical ends. The behavior of the cementation bond is proposed based on both contact tests and theoretical analyses. The bond cylinder radius is calculated by $R_b = \lambda_b R$ [28], where λ_b is the bond radius multiplier. Before a bond breaks, the bond force and moment can be updated as follows [28,32]:

$$F_n^b \leftarrow F_n^b - k_n^b \Delta \delta_n \quad (7)$$

$$F_s^b \leftarrow F_s^b - k_s^b \Delta \delta_s \quad (8)$$

$$M_r^b \leftarrow M_r^b - k_r^b \Delta \theta_r \quad (9)$$

$$M_t^b \leftarrow M_t^b - k_t^b \Delta\theta_t \tag{10}$$

where F_n^b , F_s^b , M_r^b , and M_t^b denote the transmission of normal force, tangential force, rolling moment, and twisting torque through the bond material, respectively. k_n^b , k_s^b , $k_r^b = 0.25k_n^b R_b^2$, and $k_t^b = 0.5k_s^b R_b^2$ are the normal stiffness, tangential stiffness, rolling stiffness, and twisting stiffness, respectively. $\Delta\delta_n$ is the relative normal displacement increment.

The transmission of bond force and moment is assumed to occur through different components or sections, namely A_1, B_1, C_1, C_2, B_2 , and A_2 in series, as shown in Figure 2. Hence, the bond normal stiffness can be calculated as follows [33]:

$$k_n^b = 1/(\delta_{A1} + \delta_{A2} + \delta_{B1} + \delta_{B2} + \delta_{C1} + \delta_{C2}) \tag{11}$$

$$\delta_{A1} = \frac{R_1 \zeta_E}{\pi \bar{E}^* R_b^2}$$

$$\delta_{B1} = \begin{cases} \frac{1}{2\pi \bar{E}^* (1-\eta_E) R_1 \Lambda_E} \left(\ln\left(\frac{\Lambda_E+1}{\Lambda_E-1}\right) - \ln\left(\frac{\Lambda_E+\zeta_E}{\Lambda_E-\zeta_E}\right) \right) & (\text{when } \eta_E < 1) \\ \frac{R_1(1-\zeta_E)}{\pi \bar{E}^* R_b^2} & (\text{when } \eta_E = 1) \end{cases}$$

$$\delta_{C1} = \frac{h_0^b/2}{\eta_E \pi \bar{E}^* R_b^2}$$

where δ_{A1} , δ_{B1} , and δ_{C1} are calculated by integration along the force-transmitting path, while δ_{A2} , δ_{B2} , and δ_{C2} can be obtained similarly. $\zeta_E = \sqrt{1 - (R_b/R_1)^2}$ and $\Lambda_E = \sqrt{1 + \frac{\eta_E}{1-\eta_E} (R_b/R_1)^2}$ are intermediate variables. h_0^b is the bond thickness, and $h_0^b = 0$ for a thin bond, which forms after the two particles have been in physical contact. \bar{E}^* is the bond effective modulus. Since the modulus of the bond material is smaller than that of the particles, the modulus reduction factor η_E is incorporated. The stiffness will be reduced to the parallel bond [32] when $\eta_E = 1$ and $h_0^b = 0$.

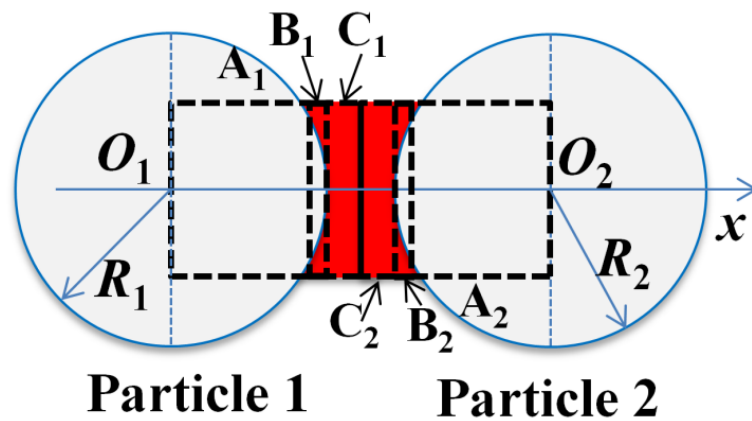


Figure 2. Stiffness calculation sketch of the bond contact.

The bond tangential stiffness can be computed as follows [28]:

$$k_s^b = k_n^b / \bar{\kappa}^* \tag{12}$$

where $\bar{\kappa}^*$ represents the ratio of normal stiffness to shear stiffness in the bond.

2.1.3. Bond Failure Criterion

Upon reaching the failure criterion, the bond undergoes breakage, resulting in abrupt reductions in force and moment in the contact to their residual values. A bond failure criterion proposed in Shen et al. [34] is simplified [33] and applied in the simulations. This bond failure criterion considers the bond size effect and the coupled effect of the

normal force, tangential force, rolling moment, and twisting torque on the bond failure. The criterion will be briefly introduced below.

The bond compressive and tensile strengths, denoted by R_{nc}^b and R_{nt}^b , respectively, are expressed as follows [34]:

$$R_{nc}^b = \chi_c \sigma_c^b A_b, \quad \chi_c = \frac{c_1}{\lambda_b c_3} \exp\left(\frac{c_2 h_0^b}{2R_b}\right) \quad (13)$$

$$R_{nt}^b = \chi_t \sigma_t^b A_b, \quad \chi_t = 1 \quad (14)$$

where $A_b = \pi R_b^2$ represents the cross-sectional area of the bond cylinder. σ_c^b represents the compressive strength, and σ_t^b signifies the tensile strength of the bond material. $\sigma_t^b = \eta_\sigma \sigma_c^b$, where η_σ represents the ratio of tensile strength to compressive strength. χ_c and χ_t are two factors considering the bond size effect, for which $c_1 = 1.45$, $c_2 = -0.7$, and $c_3 = 1/6$ were used.

The shearing, rolling, and twisting strengths, namely $R_s^b = S_s^b(R_{nc}^b + R_{nt}^b)$, $R_r^b = S_r^b(R_{nc}^b + R_{nt}^b)R_b$, and $R_t^b = S_t^b(R_{nc}^b + R_{nt}^b)R_b$, of the bond depend on the compressive strength R_{nc}^b , the tensile strength R_{nt}^b , and the bond size [34], where S_i^b ($i = s, r, t$, denoting shearing, rolling, and twisting, respectively) captures the impact of the normal force on the shearing, rolling, and twisting strengths. A simplified form of S_i^b can be expressed as follows [33,34]:

$$S_i^b = m_i f_n^b [\ln(1/f_n^b)]^{3/5} \quad (15)$$

where $f_n^b = (F_n^b + R_{nt}^b)/(R_{nc}^b + R_{nt}^b)$ is a dimensionless normal force, and the strength envelope shape parameters $m_s = 0.5$, $m_r = 0.3$, and $m_t = 0.36$ are adopted according to the data obtained by Shen et al. [34].

In general, a bond may be subjected to the normal and shear forces, rolling moment, and torque. A unified failure criterion can be characterized as follows [34]:

$$\left(\frac{\|F_s^b\|}{R_s^b}\right)^2 + \left(\frac{\|M_r^b\|}{R_r^b}\right)^2 + \left(\frac{M_t^b}{R_t^b}\right)^2 = 1 \quad (16)$$

2.2. DEM Simulations

2.2.1. Sample Preparation

The particle and particle interaction parameters that are used to prepare the uncemented sample are the same as those of the saturated sample in the work of Li et al. [30] and are shown in Table 1. In particular, at the ball–wall contacts, both the friction coefficient and the shape parameter are zero. A van der Waals force of 1.6×10^{-6} N is applied to each ball–ball contact because it cannot be neglected for silt-sized soils [4]. Figure 3 shows the grain size distribution curve of the DEM sample with a median grain size of 20 μm . An assembly is compacted in five layers via the multi-layer under-compaction method (UCM) [35]. The cubic sample is composed of 42,180 particles with a side length of 0.67 mm. When using the UCM method, the accumulated layers of the particles are compacted to an intermediate void ratio that is slightly higher than the target void ratio, 0.945, to obtain a homogenous DEM sample. Then, a vertical pressure of 12.5 kPa is applied to the top and bottom walls with the sidewalls kept stationary to reproduce an in situ K_0 stress state.

After sample preparation, the bonds were then installed at neighboring particles with a gap of less than $g_c R_b$, where g_c is the bond thickness threshold. Table 1 lists the bond parameters that were empirically set to study cemented silts in general [33]. The compressive and tensile strengths are significant parameters that control the shear strength of a cemented soil. Two representative compressive strengths, 5 MPa for weak bonds and 25 MPa for strong bonds, were analyzed in this study. Given that the experimental results

indicate a significantly lower tensile strength compared to the compressive strength, the tension-to-compression strength ratio was assumed to be 0.1.

Table 1. DEM simulation parameters.

Parameters	Values
Particle	
Particle density / $\text{kg}\cdot\text{m}^{-3}$	2710
Local damping coefficient	0.7
Particle interaction	
Effective modulus E^* /MPa	800
Normal-to-shear stiffness ratio κ^*	1.5
Friction coefficient μ	0.5
Shape parameter β	0.21
Van der Waals force F_V /N	1.6×10^{-6}
Bond contact	
Bond effective modulus \bar{E}^* /MPa	200
Bond modulus reduction factor η_E	0.2
Bond normal-to-shear stiffness ratio $\bar{\kappa}^*$	2.0
Compressive strength of the bond material σ_c^b /MPa	5; 25
Bond tension-to-compression strength ratio η_σ	0.1
Bond radius multiplier λ_b	0.35
Bond thickness threshold g_c	0.1

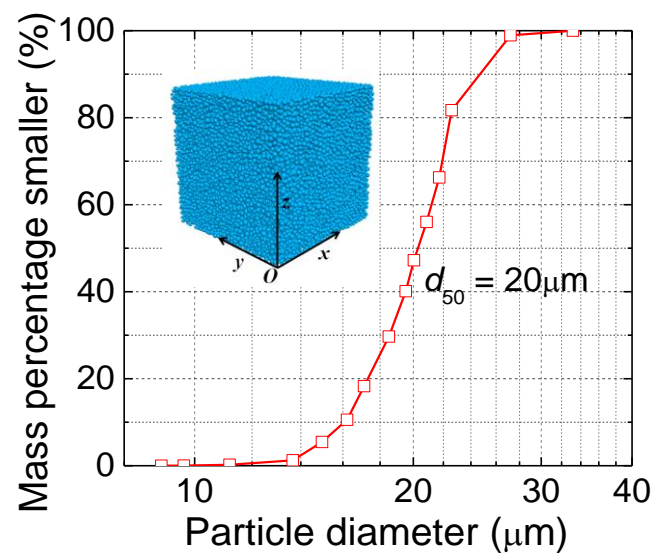


Figure 3. Grain size distribution of the DEM sample.

2.2.2. Simulation Execution

The mean stress p , deviator stress q , volumetric strain ε_v , and deviator strain ε_s are expressed as follows:

$$p = \frac{1}{3}(\sigma_1 + \sigma_2 + \sigma_3) \quad (17)$$

$$q = \frac{\sqrt{2}}{2} \sqrt{(\sigma_1 - \sigma_2)^2 + (\sigma_2 - \sigma_3)^2 + (\sigma_3 - \sigma_1)^2} \quad (18)$$

$$\varepsilon_v = \varepsilon_1 + \varepsilon_2 + \varepsilon_3 \quad (19)$$

$$\varepsilon_s = \frac{\sqrt{2}}{3} \sqrt{(\varepsilon_1 - \varepsilon_2)^2 + (\varepsilon_2 - \varepsilon_3)^2 + (\varepsilon_3 - \varepsilon_1)^2} \quad (20)$$

where σ_1 , σ_2 , and σ_3 are the principal stresses of the stress tensor, and ε_1 , ε_2 , and ε_3 are the principal strains of the strain tensor.

Following the installation of bonds, numerical samples underwent a series of tests, including constant stress ratio compression, one-dimensional compression (1D compression), conventional triaxial tests, and true triaxial tests. Figure 4 shows the stress paths in the DEM simulations. During one-dimensional compression, incremental loads were imposed on the top and bottom walls while keeping the sidewalls in a stationary position. In constant stress ratio compression (CSR compression), incremental loads were applied to the top and bottom walls, and the sidewalls were servo-controlled to maintain a constant principal stress ratio $CSR = \sigma_3 / \sigma_1$.

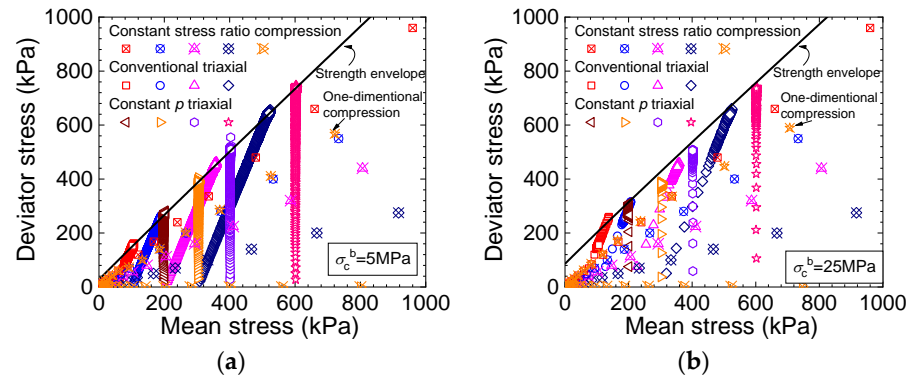


Figure 4. Stress paths in the DEM simulations: (a) $\sigma_c^b = 5$ MPa and (b) $\sigma_c^b = 25$ MPa.

In triaxial tests, following the isotropic compression of samples to various confining stresses, continuous deviator loading was initiated by downward and upward movement of the top and bottom walls. Simultaneously, the sidewalls were servo-controlled to sustain a constant horizontal stress in the conventional triaxial tests and to align the horizontal stresses with their designated target values in the true triaxial tests (constant p). The target values are determined through the following calculation:

$$\sigma_2 = \frac{(3 - 3b)p - (1 - 2b)\sigma_1}{2 - b} \quad (21)$$

$$\sigma_3 = \frac{3p - (1 + b)\sigma_1}{2 - b} \quad (22)$$

where the coefficient $b = (\sigma_2 - \sigma_3) / (\sigma_1 - \sigma_3)$.

3. Results

3.1. Bond Degradation Evolutions

The stress and strain of a granular material depend on the interparticle forces at the contacts. The average stress of a representative volume element (RVE) can be expressed as follows [36]:

$$\bar{\sigma}_{ij} = \frac{1}{V} \sum_{k=1}^N F_i^k l_j^k \quad (23)$$

where V and N are the volume and the number of contacts of the RVE, respectively; F_i^k is the contact force at contact k ; and l_j^k is the branch vector connecting the centers of the two particles.

In the disturbed state concept and damage mechanics [37] regarding cemented granular materials, it is assumed that cemented soils generally consist of bonded aggregates and unbonded grains. To evaluate the bond degradation in cemented soils subjected to external loading, a primary bond degradation variable can be defined as the ratio of the unbonded contact number to the total contact number as follows:

$$B_N = \frac{N^d}{N} \quad (24)$$

where N^d is the number of unbonded contacts.

By assuming that the applied loading is independently sustained by bonded aggregates and unbonded grains, the second bond degradation variable can be defined as the ratio of the stress sustained by the unbonded contacts to the total stress as follows:

$$B_0 = \frac{\sum_{k=1}^{N^d} F_i^k l_j^k}{\sum_{k=1}^N F_i^k l_j^k} \quad (25)$$

Under external loading, the bonded aggregates in the cemented soil gradually break and transform into unbonded grains due to the breakage of bonded contacts. The bond degradation variables B_N and B_0 represent the degree to which the soil bonding is damaged. When the bond degradation variable equals zero, the applied loading is completely sustained by the bonded aggregates, indicating that the soil bonding is intact. The bond degradation variable of the soil increases as more bonded contacts break. When the value of the bond degradation variable reaches 1.0, the soil bonding is fully disturbed; the applied stress is completely sustained by the unbonded grains.

The bond degradation is commonly assumed to vary with the plastic strain. The bond degradation mainly evolves with the volumetric plastic strain in compression tests, while it primarily develops with the deviator plastic strain in triaxial tests. Hence, an equivalent plastic strain must be introduced to consider both the volumetric and deviator plastic strains. A simple equivalent plastic strain can be defined as $\varepsilon_d^p = \sqrt{(\varepsilon_v^p)^2 + (\varepsilon_s^p)^2}$, where ε_v^p is the volumetric plastic strain and ε_s^p is the deviator plastic strain.

3.2. Compression Tests

Figure 5 shows the compression curves of the numerical samples under constant stress ratio compression with different principal stress ratios as well as the one-dimensional compression tests. For the numerical sample with weak bonds ($\sigma_c^b = 5\text{MPa}$, sample I), the void ratio first gradually decreases and then accelerates after an obvious distinguishing point, namely the “structural yield stress” point, which agrees with the experimental results [38]. In contrast, the slopes of the compression curves vary relatively gradually for the numerical sample with strong bonds ($\sigma_c^b = 25\text{MPa}$, sample II).

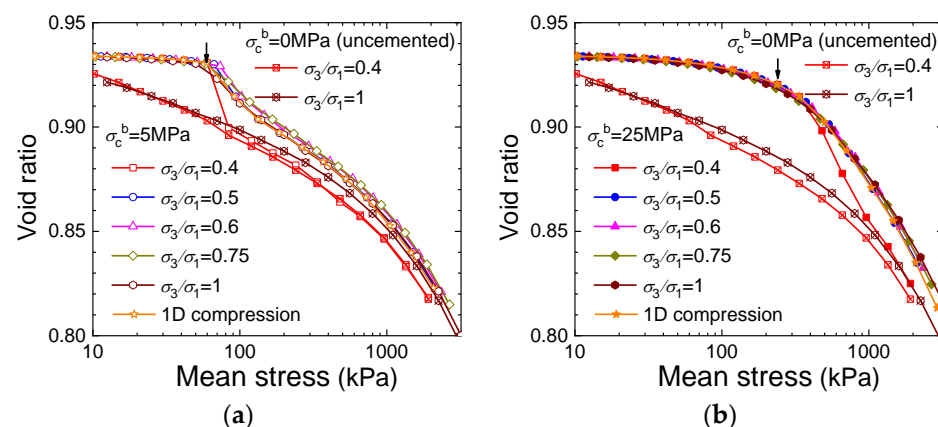


Figure 5. Compression behavior of the samples with different bond strengths: (a) $\sigma_c^b = 5\text{ MPa}$ and (b) $\sigma_c^b = 25\text{ MPa}$.

All of the specimens with different principal stress ratios are fairly coincident with each other except for the specimen with a principal stress ratio of $\sigma_3/\sigma_1 = 0.4$. Both the experimental [38,39] and DEM results illustrate that the compression curve with a small principal stress ratio is separated from the coincident curve, which is probably because

the stress state approaches the sample strength envelope. The compression curve with $\sigma_3/\sigma_1 = 0.4$ is separated from the coincident curves at a mean stress of approximately 65 kPa for sample I, while it separates at approximately 400 kPa for sample II due to the different bond strengths.

Figure 6 shows the evolution of the bond degradation variables B_N and B_0 with the equivalent plastic strain under compression tests. Both variables increase at a decreasing rate with the equivalent plastic strain until they reach 1.0 under different principal stress ratios. There is a small threshold strain, especially for sample II, with strong bonds.

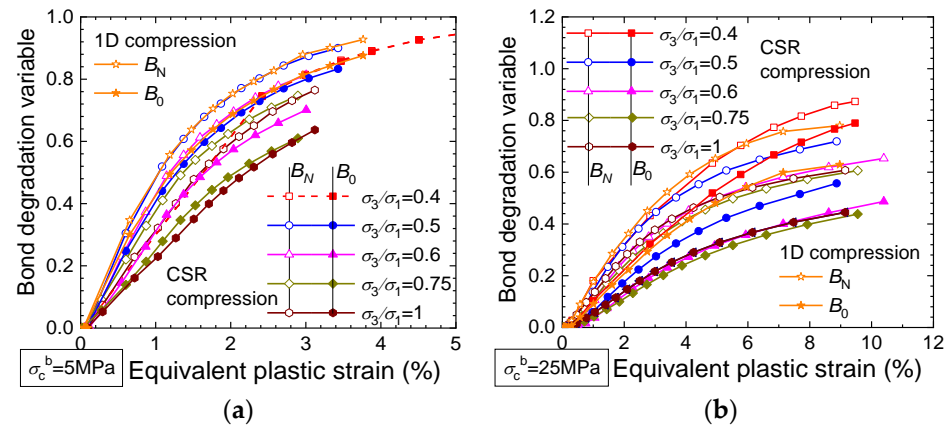


Figure 6. Evolutions of the bond degradation variables in the compression tests on the DEM samples with different bond strengths: (a) $\sigma_c^b = 5$ MPa and (b) $\sigma_c^b = 25$ MPa.

Both the principal stress ratio and the bond strength affect the evolution of the bond degradation variables. The effect of the principal stress ratio in sample II with strong bonds is more considerable than that in sample I. The bond degradation variables generally decrease as the principal stress ratio increases between 0.4 and 1.0. Except for $\sigma_3/\sigma_1 = 0.4$ in sample I, B_0 is smaller than the corresponding B_N , demonstrating the priority of the bonded contacts to sustain the applied loading throughout the compression tests.

3.3. Conventional Triaxial Tests

Figure 7 shows the relationships between the deviator stress/void ratio and axial strain observed in the conventional triaxial tests. The DEM simulation reproduces the typical behavior of cemented soils [2,40]. The deviator stress increases, and the void ratio decreases with the increase in confining stress. The strain-softening behavior increases, and the tendency for the specimens to expand increases under shearing as the bond strength increases. The deviator stresses and void ratios are almost the same for samples I and II at the critical state, which demonstrates a similar critical state for samples with different bond strengths.

Figure 8 shows the evolution of the bond degradation variables B_N and B_0 in conventional triaxial tests. There are initial equivalent plastic strains and initial bond degradation variables at the beginning of shearing for sample I under confining stresses larger than 50 kPa, which is ascribed to isotropic compression before shearing. However, the initial degradation variables are almost zero after isotropic compression for sample II on account of the large bond strength.

The evolution of the bond degradation variables in sample I with weak bonds is slightly influenced by the confining stress; some curves form a rough “S” shape under shearing. The degradation variables of the robust bonds in Sample II show an upward trend with an increasing confining stress. The degradation variable B_0 is smaller than B_N at the intermediate stage of shearing, similar to the conclusion in the compression tests, while B_0 varies near or higher than B_N at the end of shearing when the stress state develops close to the strength envelope, as illustrated by the circles in Figures 8 and 9.

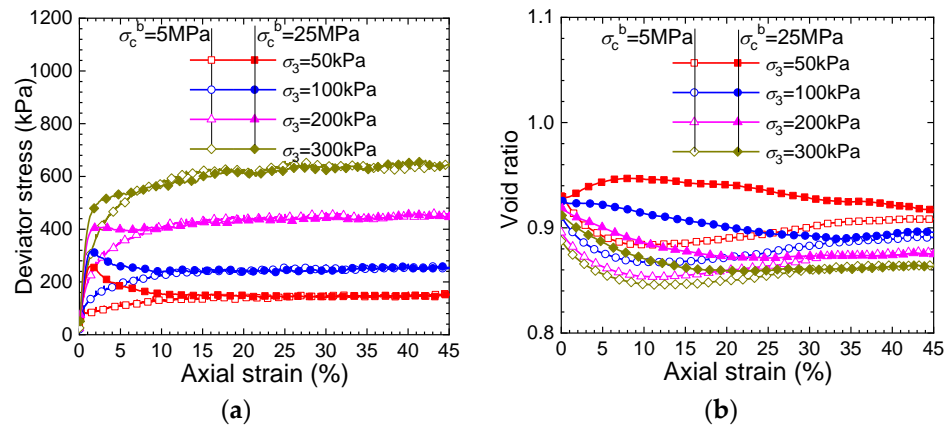


Figure 7. Stress–strain relationships and volume evolutions in the conventional triaxial tests on the DEM samples with different bond strengths: (a) stress–strain relationships and (b) volume evolutions.

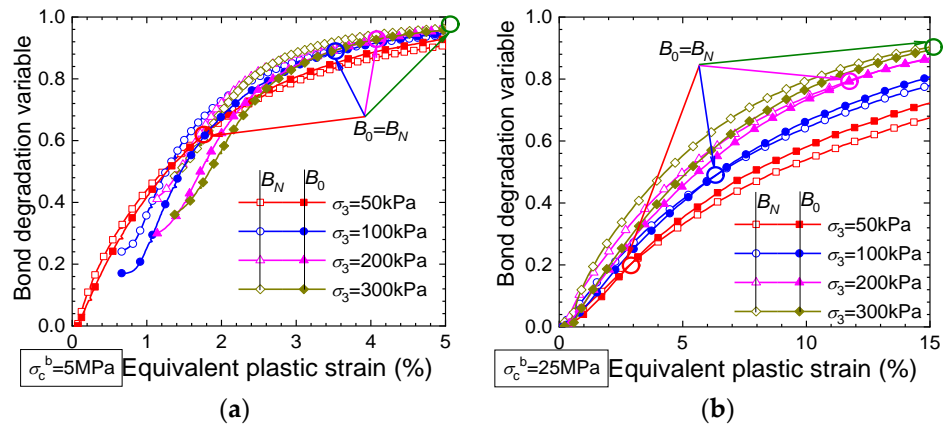


Figure 8. Evolutions of the bond degradation variables in conventional triaxial tests on the DEM samples with different bond strengths: (a) $\sigma_c^b = 5 \text{ MPa}$ and (b) $\sigma_c^b = 25 \text{ MPa}$.

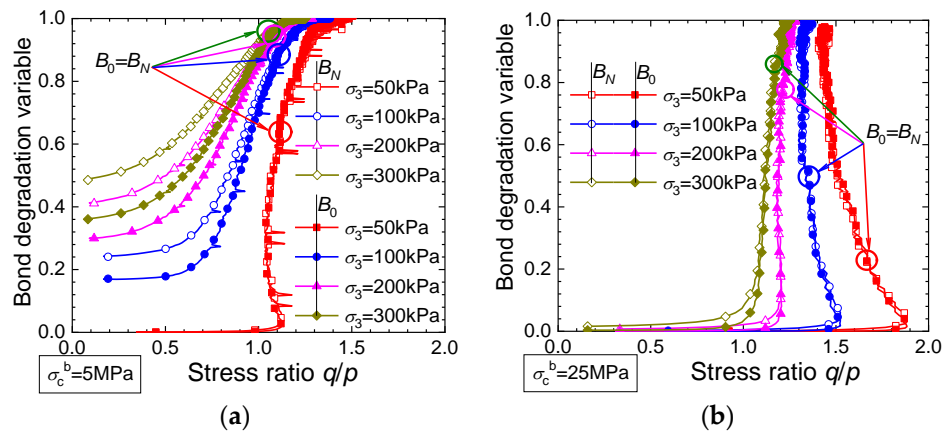


Figure 9. Relationships between the bond degradation variables and the stress ratio in the conventional triaxial tests on the DEM samples with different bond strengths: (a) $\sigma_c^b = 5 \text{ MPa}$ and (b) $\sigma_c^b = 25 \text{ MPa}$.

3.4. True Triaxial Tests

Figure 10 represents the macroscopic behavior of the numerical specimens in true triaxial tests (constant p). Parallel to the findings in conventional triaxial tests, there is an augmentation in the strain-softening behavior and an expanding tendency as the bond strength rises. In laboratory tests [41], it is noted that the deviator stress declines, and the void ratio increases with the growing coefficient $b = (\sigma_2 - \sigma_3)/(\sigma_1 - \sigma_3)$.

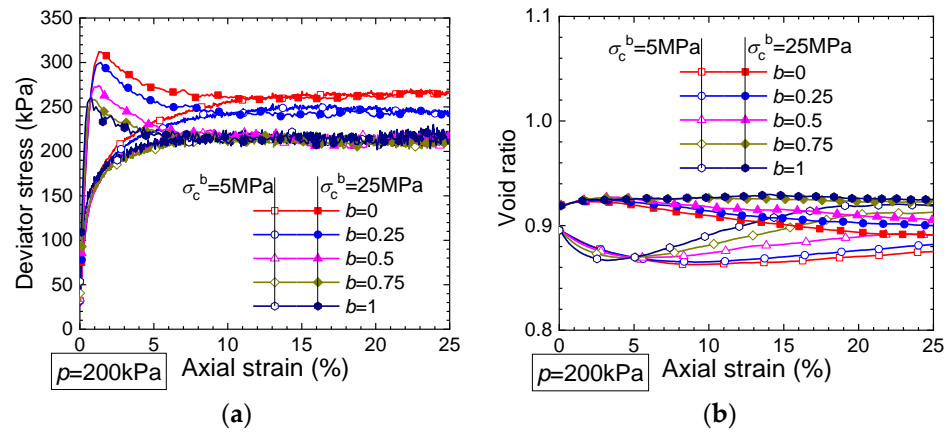


Figure 10. Stress–strain relationships and volume evolutions in the true triaxial tests on the DEM samples with different bond strengths: (a) stress–strain relationships and (b) volume evolutions.

Figure 11 shows the evolution of the bond degradation variables B_N and B_0 in the true triaxial tests. The degradation variables increase with the equivalent plastic strain, forming a rough “S” shape for sample I with weak bonds, and increase at a decreasing rate for sample II with strong bonds. The bond degradation variables are slightly influenced by the coefficient b for sample I, while they decrease considerably as the coefficient b increases for sample II. The degradation variable B_0 tends to be near or higher than B_N at the end of shearing, especially for the samples with a small confining stress and small coefficient b .

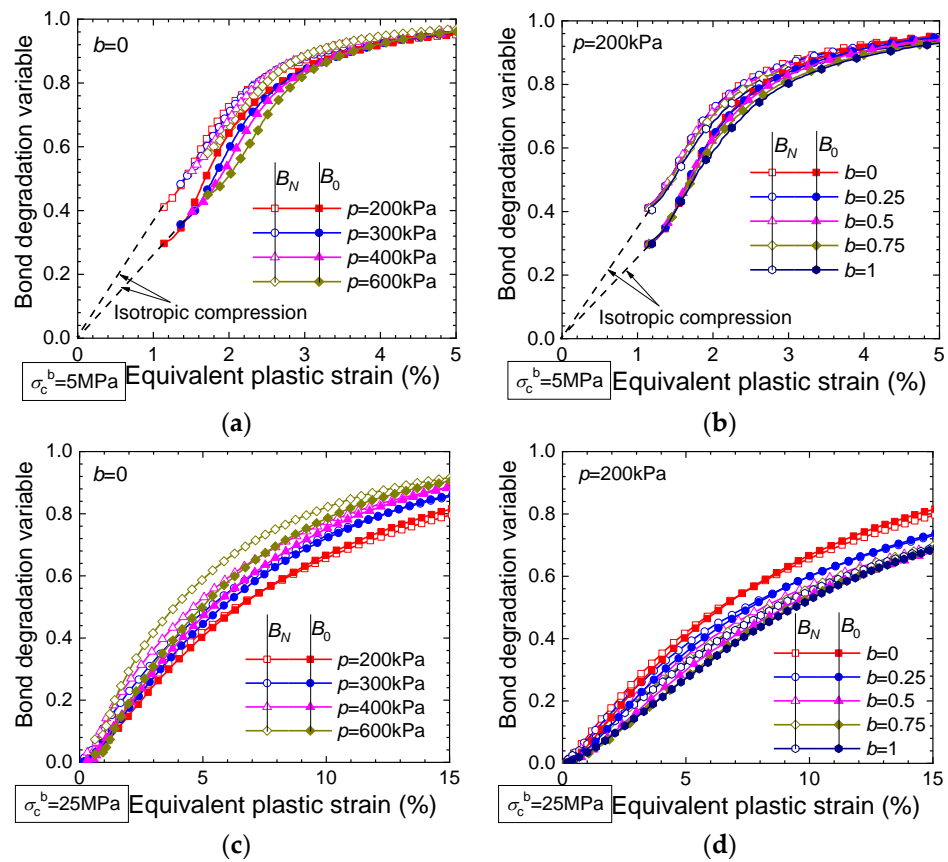


Figure 11. Evolutions of the bond degradation variables in true triaxial tests on the DEM samples with different bond strengths: (a,b) $\sigma_c^b = 5$ MPa and (c,d) $\sigma_c^b = 25$ MPa.

4. Discussion

The evolution of the bond degradation variables B_N and B_0 with the equivalent plastic strain appears to be affected by the ratio of principal stresses, confining stress, and coefficient b , especially for samples with strong bonds. Hence, there is a defect in using a general bond degradation evolution law, e.g., B_N or $B_0 = f(\epsilon_d^p)$, in constitutive modeling since the parameters in the formula are dependent on the stress path. It is necessary to further develop a stress-path-independent bond degradation variable.

The stress ratio and strength potential are incorporated into B_0 to derive a bond degradation variable B_σ that considers their effect on the bond degradation evolution as follows:

$$B_\sigma = \frac{2B_0}{1 + (\eta/\eta_f)^2} \tag{26}$$

where $\eta = q/p$ is the stress ratio, $\eta_f = q_f/p$ is the strength potential, and q_f is the deviator stress at failure. η_f can be expressed by an extended elliptical envelope:

$$\eta_f = \max\left(M\left(\frac{p + p_t}{p}\right)\left(\frac{p_c}{p + p_t} - 1\right)^{1/n}, M\right) \tag{27}$$

The envelope, in which the parameters are determined using conventional triaxial tests, is shown in Figure 4 for both samples I and II. In the expression of B_σ , η/η_f is incorporated to accommodate the bond degradation rate.

Figure 12 shows the collective evolution of the bond degradation variables B_0 and B_σ with the equivalent plastic strain under all of the above stress paths. The impact of the stress path on the evolution of the bond degradation variable B_σ seems to be less pronounced compared to that on B_0 . The collective data of B_σ can be effectively fitted using the following exponential formulation and hyperbolic formulation:

$$B_\sigma = 1 - \exp[-c_a(\epsilon_d^p)^{c_b}] \tag{28}$$

$$B_\sigma = \frac{\epsilon_d^p}{h_a + h_b \epsilon_d^p} \tag{29}$$

where c_a represents the increasing rate of B_σ , and c_b is an index. $1/h_a$ controls the increasing rate of B_σ , and $1/h_b$ represents the ultimate value of B_σ . Figure 12c,d show the fitting curves of both formulations.

In constitutive modeling, one-dimensional compression and conventional triaxial tests are recommended to determine the parameters in the evolution law of the bond degradation variable B_σ for simplicity.

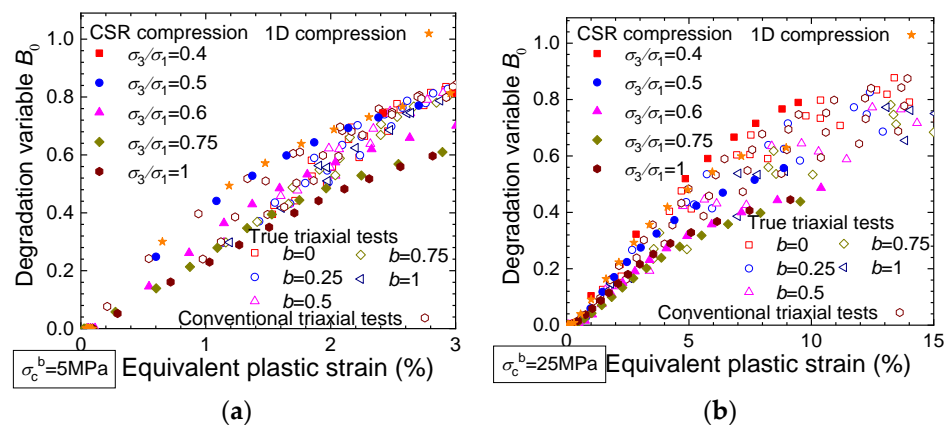


Figure 12. Cont.

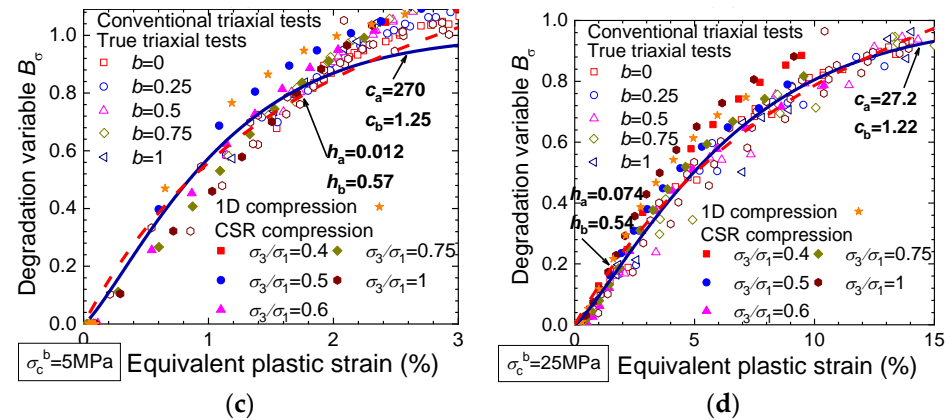


Figure 12. Overview of the evolution of the bond degradation variables: (a,b) variable B_0 and (c,d) variable B_σ .

5. Conclusions

This paper investigates the bond degradation evolution of cemented soils at the particle and contact scales. Numerical compression and triaxial tests reproduced the primary experimental mechanical behavior. Then, the simulation results were used to investigate the evolution of the bond degradation variables B_N and B_0 . A stress-path-independent bond degradation variable B_σ was developed based on B_0 , and its evolution law was formulated accordingly. The conclusions are as follows:

- (1) The bond degradation variables B_N , B_0 , and B_σ represent the extent to which the soil bonding is damaged. A degradation variable of 0/1.0 indicates that the applied stress is completely sustained by the bonded aggregates/unbonded grains.
- (2) The bond degradation variables B_N and B_0 increase with the equivalent plastic strain until they reach 1.0 under varying stress paths. The evolutions of both variables are influenced by the principal stress ratio, confining stress, and coefficient b , especially for the sample with strong bonds.
- (3) In compression tests with principal stress ratios higher than 0.4, B_0 is smaller than the corresponding B_N , indicating the priority of the bonded contacts to sustain the applied loads. In triaxial tests, B_0 is smaller than B_N before the intermediate stage of shearing, and then B_0 evolves to be near or larger than B_N at the end of shearing when the stress state approaches the strength envelope.
- (4) The evolutions of the further developed bond degradation variable B_σ under different stress paths are approximately coincident with each other. The collective data of B_σ can be effectively fitted by an exponential or a hyperbolic evolution law.

In the future, the evolution of the bond degradation variables for unsaturated structured soils will be studied by taking capillary forces into account. A micromechanical-based constitutive model for cemented soils can be developed by incorporating the evolution law of the bond degradation variable.

Author Contributions: Writing—original draft and review and editing, J.H.; writing—original draft and review and editing, T.L. and Y.R. All authors have read and agreed to the published version of the manuscript.

Funding: This work was financially supported by the China National Natural Science Foundation (No. 51809193) and the China Postdoctoral fund (No. 2019M651580). These supports are greatly appreciated.

Data Availability Statement: The data associated with this research are available from the corresponding author upon reasonable request.

Conflicts of Interest: The authors declare that they have no known competing financial interests or personal relationships that could have appeared to influence the work reported in this paper.

Abbreviations

R_c	contact radius of particle interaction
β	shape parameter
R	common radius of a particle pair
F_v	van der Waals force
F_n^p	normal force of particle interaction
F_s^p	tangential force of particle interaction
M_r^p	rolling moment of particle interaction
M_t^p	twisting torque of particle interaction
k_n	normal stiffness of particle interaction
k_s	tangential stiffness of particle interaction
k_r	rolling stiffness of particle interaction
k_t	twisting stiffness of particle interaction
δ_n	normal overlap between a particle pair
$\Delta\delta_s$	relative shear displacement increment
$\Delta\theta_r$	relative rotation increment
$\Delta\theta_t$	relative twist increment
μ	friction coefficient between a particle pair
E^*	interparticle effective modulus
κ^*	normal-to-shear stiffness ratio
λ_b	bond radius multiplier
R_b	bond radius
F_n^b	bond normal force
F_s^b	bond tangential force
M_r^b	bond rolling moment
M_t^b	bond twisting torque
k_n^b	bond normal stiffness
k_s^b	bond tangential stiffness
k_r^b	bond rolling stiffness
k_t^b	bond twisting stiffness
$\Delta\delta_n$	relative normal displacement increment
h_0^b	bond thickness
\bar{E}^*	bond effective modulus
η_E	bond modulus reduction factor
$\bar{\kappa}^*$	bond normal-to-shear stiffness ratio
σ_c^b	compressive strength of the bond material
σ_t^b	tensile strength of the bond material
R_{nc}^b	bond compressive strength
R_{nt}^b	bond tensile strength
η_σ	bond tension-to-compression strength ratio
R_s^b	bond shearing strength
R_r^b	bond rolling strength
R_t^b	bond twisting strength
g_c	bond thickness threshold
σ_1, σ_2 and σ_3	principal stresses of a stress tensor
$\varepsilon_1, \varepsilon_2$ and ε_3	principal strains of a strain tensor
p	mean stress
q	deviator stress
ε_v	volumetric strain
ε_s	deviator strain
$\bar{\sigma}_{ij}$	average stress tensor of a representative volume element
B_N	bond degradation variable based on the number of unbonded contacts
B_0	bond degradation variable based on the stress contribution of unbonded contacts
ε_d^p	equivalent plastic strain
ε_v^p	volumetric plastic strain
ε_s^p	deviator plastic strain
B_σ	bond degradation variable considering stress effect

η	stress ratio
η_f	strength potential
p_c	yield surface size of a cemented soil
p_{c0}	yield surface size of corresponding uncemented soil

References

- Mitchell, J.K. *Fundamentals of Soil Behavior*; Wiley: New York, NY, USA, 1976.
- Leroueil, S.; Vaughan, P.R. The general and congruent effects of structure in natural soils and weak rocks. *Géotechnique* **1990**, *40*, 467–488. [[CrossRef](#)]
- Burland, J.B. On the compressibility and shear strength of natural clays. *Géotechnique* **1990**, *40*, 329–378. [[CrossRef](#)]
- Yang, R.Y.; Zou, R.P.; Yu, A.B. Computer simulation of the packing of fine particles. *Phys. Rev. E* **2000**, *62*, 3900–3908. [[CrossRef](#)] [[PubMed](#)]
- Zourmpakis, A.; Boardman, D.; Rogers, C.; Jefferson, I.; Gunn, D.; Jackson, P.; Northmore, K.; Entwisle, D.; Nelder, L.; Dixon, N. Case study of a loess collapse field trial in Kent, SE England. *Q. J. Eng. Geol. Hydrogeol.* **2006**, *39*, 131–150. [[CrossRef](#)]
- Xu, L.; Dai, F.C.; Tham, L.G.; Tu, X.B.; Min, H.; Zhou, Y.F.; Wu, C.X.; Xu, K. Field testing of irrigation effects on the stability of a cliff edge in loess, North-west China. *Eng. Geol.* **2011**, *120*, 10–17. [[CrossRef](#)]
- Yu, H.S.; Tan, S.M.; Schnaid, F. A critical state framework for modelling bonded geomaterials. *Geomech. Geoengin. Int. J.* **2007**, *2*, 61–74. [[CrossRef](#)]
- Nova, R.; Castellanza, R.; Tamagnini, C. A constitutive model for bonded geomaterials subject to mechanical and/or chemical degradation. *Int. J. Numer. Anal. Mech. Geomech.* **2003**, *27*, 705–732. [[CrossRef](#)]
- Asaoka, A.; Nakano, M.; Noda, T. Superloading yield surface concept for highly structured soil behavior. *Soils Found* **2000**, *40*, 99–110. [[CrossRef](#)]
- Zhu, E.Y.; Yao, Y.P. Structured UH model for clays. *Transp. Geotech.* **2015**, *3*, 68–79. [[CrossRef](#)]
- Liu, W.H.; Li, W.G.; Zhang, H.Y.; Lin, X.Y.; Kong, G.Q.; Wang, L.; Hu, P. A critical state constitutive model for unsaturated structured soils. *Comput. Geotech.* **2022**, *152*, 104993. [[CrossRef](#)]
- Desai, C.S.; Toth, J. Disturbed state constitutive modeling based on stress-strain and nondestructive behavior. *Int. J. Solids Struct.* **1996**, *33*, 1619–1650. [[CrossRef](#)]
- Wu, Z.; Xu, J.; Li, Y.; Wang, S. Disturbed state concept-based model for the uniaxial strain-softening behavior of fiber-reinforced soil. *Int. J. Geomech.* **2022**, *22*, 04022092. [[CrossRef](#)]
- Shen, Z.J. An elasto-plastic damage model for cemented clays. *Chin. J. Geotech. Eng.* **1993**, *15*, 21–28. (In Chinese)
- Jiang, M.J.; Zhang, F.G.; Sun, Y.G. An evaluation on the degradation evolutions in three constitutive models for bonded geomaterials by DEM analyses. *Comput. Geotech.* **2014**, *57*, 1–16. [[CrossRef](#)]
- Nemat-Nasser, S.; Okada, N. Radiographic and microscopic observation of shear bands in granular materials. *Géotechnique* **2001**, *51*, 753–765. [[CrossRef](#)]
- White, D.; Take, W.A.; Bolton, M.D. Soil deformation measurement using particle image velocimetry (PIV) and photogrammetry. *Géotechnique* **2003**, *53*, 619–631. [[CrossRef](#)]
- Andò, E.; Hall, S.A.; Viggiani, G.; Desrues, J.; Bésuelle, P. Experimental micromechanics: Grain-scale observation of sand deformation. *Geotech. Lett.* **2012**, *2*, 107–112. [[CrossRef](#)]
- Cundall, P.A.; Strack, O.D.L. A discrete numerical model for granular assemblies. *Géotechnique* **1979**, *29*, 47–65. [[CrossRef](#)]
- Wang, Y.H.; Leung, S.C. A particulate-scale investigation of cemented sand behavior. *Can. Geotech. J.* **2008**, *45*, 29–44. [[CrossRef](#)]
- Jiang, M.J.; Li, T.; Hu, H.J.; Thornton, C. DEM analyses of one-dimensional compression and collapse behaviour of unsaturated structural loess. *Comput. Geotech.* **2014**, *60*, 47–60. [[CrossRef](#)]
- Cohen, E.; Klar, A. Micromechanical modeling of the effect of dissociation on the mechanical response of hydrate-bearing sediments. *Granul. Matter* **2022**, *24*, 84. [[CrossRef](#)]
- Li, T.; Li, L.; Liu, J.; Zhou, H. Influence of hydrate participation on the mechanical behaviour of fine-grained sediments under one-dimensional compression: A DEM study. *Granul. Matter* **2022**, *24*, 32. [[CrossRef](#)]
- He, J.; Zhu, H.; Zhou, M. DEM-Based Study on the Mechanical Behaviors of Pore-Filling MHBS under Drained True Triaxial Conditions Varying the Intermediate Stress Ratio of Constant Mean Effective Stresses. *Int. J. Geomech.* **2022**, *22*, 04022132. [[CrossRef](#)]
- He, J.; Li, T.; Rui, Y. Geomechanical Properties of Deep-Sea Pore-Filled Methane Hydrate-Bearing Soils at Critical State Using DEM Analysis. *Fractal Fract.* **2023**, *7*, 681. [[CrossRef](#)]
- Thornton, C. Numerical simulations of deviatoric shear deformation of granular media. *Géotechnique* **2000**, *50*, 43–53. [[CrossRef](#)]
- Jiang, M.J.; Liu, J.D.; Arroyo, M. Numerical evaluation of three non-coaxial kinematic models using the distinct element method for elliptical granular materials. *Int. J. Numer. Anal. Mech. Geomech.* **2016**, *40*, 2468–2488. [[CrossRef](#)]
- Itasca Particle Flow Code: User's Manual. 2014. Available online: <http://www.itascacg.com> (accessed on 14 February 2024).
- Jiang, M.J.; Shen, Z.F.; Wang, J.F. A novel three-dimensional contact model for granulates incorporating rolling and twisting resistances. *Comput. Geotech.* **2015**, *65*, 147–163. [[CrossRef](#)]
- Li, T.; Jiang, M.J.; Thornton, C. Three-dimensional discrete element analysis of triaxial tests and wetting tests on unsaturated compacted silt. *Comput. Geotech.* **2018**, *97*, 90–102. [[CrossRef](#)]

31. Li, T.; Jiang, M.; Li, L. DEM Analysis of Mechanical Behavior of Unsaturated Silt under Strain-Controlled Constant Stress Ratio Compression Tests. *Int. J. Geomech.* **2021**, *21*, 04021197. [[CrossRef](#)]
32. Potyondy, D.O.; Cundall, P.A. A bonded-particle model for rock. *Int. J. Rock Mech. Min.* **2004**, *41*, 1329–1364. [[CrossRef](#)]
33. Li, T. Three-Dimensional DEM Simulation and Constitutive Model of Unsaturated Structural Loess. Ph.D. Thesis, Tongji University, Shanghai, China, 2017. (In Chinese).
34. Shen, Z.F.; Jiang, M.J.; Wan, R. Numerical study of inter-particle bond failure by 3D discrete element method. *Int. J. Numer. Anal. Mech. Geomech.* **2016**, *40*, 523–545. [[CrossRef](#)]
35. Jiang, M.J.; Konrad, J.M.; Leroueil, S. An efficient technique for generating homogeneous specimens for DEM studies. *Comput. Geotech.* **2003**, *30*, 579–597. [[CrossRef](#)]
36. Bagi, K. Stress and strain in granular assemblies. *Mech. Mater.* **1996**, *22*, 165–177. [[CrossRef](#)]
37. Shen, Z.J. Breakage mechanics for geological materials: An ideal brittle-elasto-plastic model. *Chin. J. Geotech. Eng.* **2003**, *25*, 253–257. (In Chinese)
38. Hu, Z.Q. Inundation Deformation Test and Numerical Analysis on Loess Structural Model and Loess Canal. Ph.D. Thesis, Xi'an University of Technology, Xi'an, China, 2000. (In Chinese).
39. Charles, J.A. The use of one-dimensional compression tests and elastic theory in predicting deformations of rockfill embankments. *Can. Geotech. J.* **1976**, *13*, 189–200. [[CrossRef](#)]
40. Maccarini, M. Laboratory Studies of Weakly Bonded Artificial Soil. Ph.D. Thesis, University of London, London, UK, 1987.
41. Callisto, L.; Rampello, S. Shear strength and small-strain stiffness of a natural clay under general stress conditions. *Géotechnique* **2002**, *52*, 547–560. [[CrossRef](#)]

Disclaimer/Publisher's Note: The statements, opinions and data contained in all publications are solely those of the individual author(s) and contributor(s) and not of MDPI and/or the editor(s). MDPI and/or the editor(s) disclaim responsibility for any injury to people or property resulting from any ideas, methods, instructions or products referred to in the content.